Presented at the 29th European PV Solar Energy Conference and Exhibition, 22-26 September 2014, Amsterdam, The Netherlands

THE HIP-MWT+ SOLAR CELL CONCEPT ON N-TYPE SILICON AND METALLIZATION-INDUCED VOLTAGE LOSSES

E. Lohmüller, S. Werner, B. Thaidigsmann, N. Wöhrle, S. Mack, F. Clement, D. Biro
Fraunhofer Institute for Solar Energy Systems ISE, Heidenhofstraße 2, 79110 Freiburg, Germany
Phone: +49 761 - 4588 5701, e-mail: elmar.lohmueller@ise.fraunhofer.de

ABSTRACT: We present high-performance metal wrap through+ (n-HIP-MWT+) solar cells (239 cm² area) on n-type Czochralski-grown silicon (Cz-Si) wafers with a boron-doped front-side emitter. Peak conversion efficiencies of η = 19.5 % are measured using a black chuck. Short-circuit current density j_{SC}, open-circuit voltage V_{OC}, and fill factor *FF* are 39.6 mA/cm², 650 mV, and 75.7 %, respectively. The loss in V_{OC}, caused by front and rear side metallization, is found to be 16 mV for the n-HIP-MWT+ as well as for H-pattern cells with electrical non-contacting busbars fabricated in parallel, whereas the use of electrical contacting busbars in case of the H-pattern cells leads to a significantly higher V_{OC} loss of 24 mV. The saturation current density underneath the front silver-aluminum (Ag-Al) contacts is determined to be $j_{0,met,Ag\text{-}Al} \approx 3500$ fA/cm², which is three times larger than $j_{0,met,Ag}$ found for the silver contacts on the rear side. The high $j_{0,met,Ag\text{-}Al}$ values are assumed to originate from deep spikes formed during Ag-Al paste contact firing. This assumption is supported by numerical simulations performed with *Sentaurus Device*.
Keywords: H-pattern, metallization, MWT, n-type silicon solar cells, spikes, recombination.

1 INTRODUCTION

Since the introduction of the metal wrap through (MWT) concept by Kerschaver et al. in 1998 [1], the MWT technology improved significantly.

Focus was mostly set on the use of p-type silicon as base material for this back-contacted cell technology. A wide range of different p-type MWT cell structures have been developed, mainly differing in the structural configuration of the wafer's rear side and emitter [2]. Initially, an additional emitter—at the rear side and inside the vias—was necessary to provide electrical contact separation/insulation between base and external n-type contacts. However, with the development of special electrical non-contacting silver pastes, or so-called via pastes [3–5], the role of this emitter has become dispensable [2,3,6]. One of these novel cell concepts is the p-type high-performance MWT+ (HIP-MWT+) structure [2], which is known for its high conversion efficiencies above 20 % on large-area wafers [2,7]. In this structure, no emitter is present at the rear side and inside the vias.

However, one drawback of boron-doped p-type Czochralski-grown silicon (Cz-Si) is that it suffers from light-induced degradation, as boron-oxygen complexes are activated upon illumination [8]. The conversion efficiency in the degraded state can be significantly lower than in the annealed state. To overcome this issue, the use of phosphorus-doped n-type Cz-Si is an option [9].

In 2010, first large-area MWT solar cells using n-type Cz-Si as base material were reported by Guillevin et al. [10]. Recently, they reported peak conversion efficiencies reaching 20 % [11]. However, a detailed description of the realized MWT cell structure is still pending. On the other hand, we reported a first transition of the HIP-MWT structure (still featuring an emitter within the vias) from p-type to n-type Cz-Si in 2013 [12]. At the beginning of this year, we were able to fabricate the first HIP-MWT+ solar cells using n-type Cz-Si wafers with conversion efficiencies reaching up to 19 % [13]. Such a dynamic progress points out the large potential of the rather new n-type MWT solar cell technology.

Main challenges for n-type solar cells with a boron-doped front-side emitter are recombination losses caused by the silver-aluminum (Ag-Al) metallization pastes currently being used [14,15]. One option to decrease these losses is the reduction of the overall metallized area on the cell's front side, what is an inherent property of the MWT concept. Another option is the formation of a deeper junction below the contacts [14,15] by, for example, using the selective emitter technology [15,16].

This work focuses on two subject matters: i) the n-type HIP-MWT+ solar cell concept (hereinafter referred to as n-HIP-MWT+), depicted in Fig. 1b, and ii) the reduction of metallization-induced recombination losses on the cell's front side by decreasing the contacted area. Therefore, n-type H-pattern cells (Fig. 1a) are fabricated with electrical contacting or non-contacting busbars.

Concerning point one, the relocation of the external front contacts to the rear side triggers challenges in the n-HIP-MWT+ concept in comparison with the H-pattern structure. These challenges are briefly discussed in section 2. In the subsequent sections, design and manufacturing processes for the H-pattern and the n-HIP-MWT+ cells are reviewed and the results of current-voltage (*I-V*) measurements are discussed. By comparison with the simultaneously fabricated H-pattern cells, the n-HIP-MWT+ cell structure is evaluated.

(a) H-pattern

(b) n-HIP-MWT+

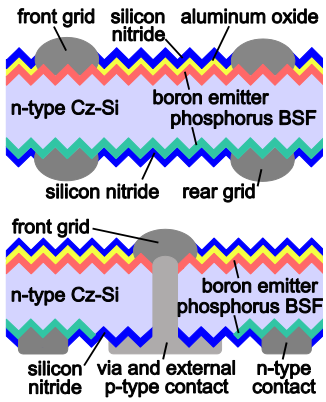

Figure 1: Schematic cross sections of the investigated n-type Cz-Si cell structures: (a) the H-pattern structure; (b) the n-HIP-MWT+ structure, which denotes an n-type MWT cell with an emitter neither inside the vias nor at the rear side. No phosphorus-doped back surface field (BSF) is present below the external p-type contact pads.

Point two of this work is concerned with the quantification of open-circuit voltage losses due to metallization with the currently used screen printing pastes. By determination of saturation current densities j_0 of the passivated doped front and rear sides as well as the base, an upper limit is calculated for the achievable open-circuit voltage $V_{OC,limit}$. This value is compared to the implied open-circuit voltages iV_{OC} measured on some of the cells prior to metallization. By calculating the difference between iV_{OC} and V_{OC} of finished cells, the total voltage loss due to recombination underneath the metal contacts (sum of front and rear side) is quantified. Subsequently, an estimation of saturation current densities below the metal contacts $j_{0,met}$ for front and rear sides is performed. Finally, a numerical simulation is used to propose a possible explanation for the occurrence of high $j_{0,met,Ag\text{-}Al}$ values caused by the Ag-Al paste used on the cell's front side.

2 THE N-HIP-MWT+ CELL STRUCTURE

As shown in Fig. 1b, the n-HIP-MWT + cell structure neither has an emitter on the rear side nor inside the vias nor does it have a phosphorus-doped back surface field (BSF) below the external p-type contact pads. To prevent shunting between via metallization—which consists of the via and the external p-type contact pad—and the adjacent n-type-doped region, an electrical non-contacting via paste is essential [3,5,11,13].

Since partial shading of a photovoltaic module can lead to reverse biasing the shaded cells [17], it is important that those cells are not harmed by the applied negative voltage and that the reverse behavior is not detrimental to the module. This has already been proven for n-type Cz-Si MWT solar cells with cell structures similar or identical to the n-HIP-MWT+ concept [11,13]. The challenges concerning reverse bias behavior are found to be comparable with those of common n-type Cz-Si H-pattern cells. Several works show that in n-type Cz-Si solar cells in general, currents occurring under reverse bias I_{rev} are strongly dependent on the fabrication process and can be significantly higher than those observed for p-type Cz-Si solar cells [11,13,18–20]. On the other hand, low currents of I_{rev} < 1 A at a voltage of -12 V have been reported for n-type Cz-Si H-pattern as well as n-type Cz-Si MWT solar cells [11,20]. Also, no significant influence of reverse biasing on the forward *I-V* characteristics has been observed for both cell types [11,13].

3 SOLAR CELL FABRICATION

The H-pattern and the n-HIP-MWT+ solar cells are fabricated using pseudo-square n-type Cz-Si wafers with an edge length of 156 mm, a diameter of 200 mm, an initial thickness of 205 µm, and a specific base resistivity of $\rho_{base} \approx 1.5$ Ωcm.

3.1 Metallization layout

The photographs in Fig. 2 show the metallization layouts on the front and back side for both cell types. The H-pattern cells feature three busbars (Fig. 2a), whereas a four-busbar layout is used for the n-HIP-MWT+ cells (Fig. 2b). The percentage of metallized front and rear area is discussed in section 3.4.

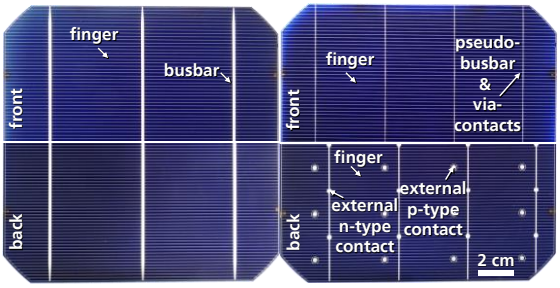

(a) H-pattern (b) n-HIP-MWT+

Figure 2: Photographs of front (top) and back (bottom) of n-type Cz-Si (a) H-pattern and (b) n-HIP-MWT+ solar cells with 156 mm edge length. For each external p-type contact pad in (b), two metallized vias transfer the current from front to back.

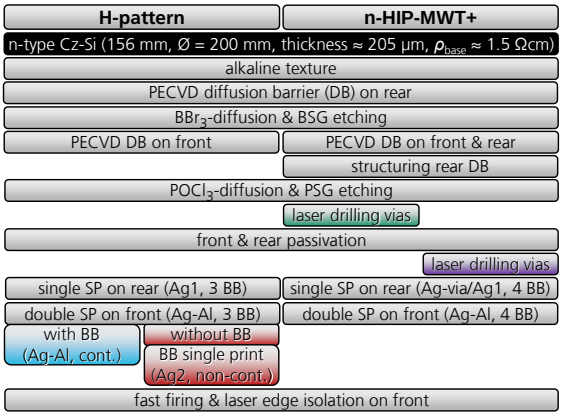

Figure 3: Process sequence for fabrication of the n-type Cz-Si H-pattern and n-HIP-MWT+ solar cells shown in Fig. 1 and Fig. 2 (SP: screen printing, BB: busbar).

3.2 Process sequence

The cells are fabricated according to the procedure depicted in Fig. 3. Following alkaline texturing, the differently doped front and rear sides are formed by atmospheric pressure tube furnace diffusion processes with first, a boron tribromide (BBr_3), and then a phosphorus oxychloride ($POCl_3$) source. The necessary diffusion barrier layers are formed by plasma-enhanced chemical vapor deposition (PECVD) [21]. For the n-HIP-MWT+ cells, the rear-side diffusion barrier is structured prior to $POCl_3$-diffusion using inkjet-printed masking resist and buffered hydrofluoric acid (HF). In each case, the borosilicate glass (BSG) and phosphosilicate glass (PSG) are removed in HF solution along with the diffusion barrier layers.

The resulting front- and rear-side sheet resistances after BBr_3- and $POCl_3$-diffusion are $R_{sh} \approx 70$ Ω/sq and $R_{sh} \approx 60$ Ω/sq, respectively. During $POCl_3$-diffusion, the boron doping profile does not alter significantly [21]. The resulting doping profiles, shown in Fig. 4, are determined by electrochemical capacitance-voltage (ECV) measurements [22] on wafers with alkaline saw damaged etched surfaces. The boron emitter features a maximum dopant concentration of $N_{max} \approx 1.0 \cdot 10^{20}$ cm^{-3} and a profile depth of $d \approx 480$ nm. For the phosphorus BSF, the values are given by $N_{max} \approx 2.1 \cdot 10^{20}$ cm^{-3} and $d \approx 780$ nm.

Laser-drilling the vias of the n-HIP-MWT+ cells is performed either i) before passivation followed by wet chemical cleaning, or ii) after passivation without any post treatment. The front passivation and anti-reflective

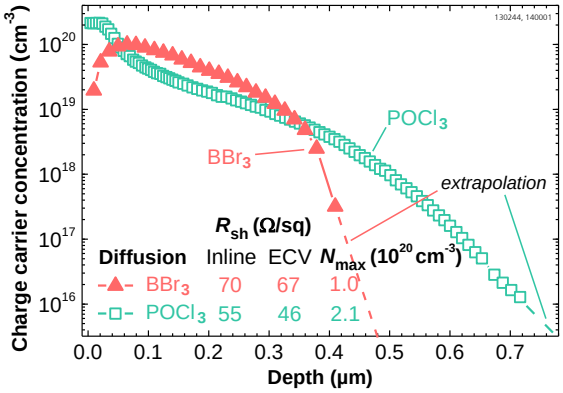

Figure 4: Charge carrier concentration profiles determined by ECV measurements in the center of Cz-Si wafers with alkaline saw damage etched surfaces. The parameter N_{max} denotes the maximum dopant concentration. The profile depths are estimated by extrapolation (dashed lines) to a doping concentration of $3.2 \cdot 10^{15}$ cm^{-3}, which correlates to the base doping concentration. Also shown are the sheet resistances R_{sh}, either measured by inductive coupling at an inline measurement tool (Inline) [24], or calculated from the doping profiles (ECV) by using Klaassen's carrier mobility model [25].

coating consists of a thin aluminum oxide layer applied by fast atomic layer deposition [23] and a PECVD silicon nitride (SiN_x) layer. The rear side is passivated by a PECVD SiN_x layer.

For determination of iV_{OC} values, two cells per group are additionally fired and measured with quasi-steady state photo conductance (QSSPC) prior to metallization. This fast firing process is identical to the fast firing process used later for the cells after metallization (same conveyor belt velocity and set peak temperature).

For screen printing, commercial metal pastes are used. The rear side metallization of the H-pattern cells (see Fig. 1a and Fig. 2a) is screen printed with a three-busbar layout (fingers and busbars) using a fire-through and contacting silver paste (paste Ag1; see also Table I). The front is also metallized with a three-busbar layout with a variation in busbar metallization. For the first group, the finger and the busbar contacts are simultaneously double-printed with a fire-through and electrical contacting Ag-Al paste. For the second group, only the finger contacts are double-printed with the Ag-Al paste, followed by single-printing the busbar contacts with a non-fire-through and electrical non-contacting silver paste (paste Ag2).

For the rear side of the n-HIP-MWT+ cells (see Fig. 1b and Fig. 2b), a two-step screen printing process is used. In the first step, the external p-type contact pads and the vias are metallized with a non-fire-through and non-contacting silver via paste (paste Ag-via) [3,5]. In the second step, the finger and the external n-type contacts are printed with the contacting silver paste Ag1. The front grid with fingers and four thin pseudo-busbars is double-printed with the contacting Ag-Al paste.

Finally, the contact formation with the same process conditions for all fabricated cells is performed in a fast firing furnace, followed by laser edge isolation on the front side.

Table I: Metallized surface area for the different metal structures for both cell types. The values are calculated based on measured structure sizes. For the H-pattern cells either the front metal structures marked with # or * are applied (BB: busbar).

Cell type	Side	Metal structures	Paste type	Metallized area (%)
H-pattern	front#	fingers+BBs	Ag-Al	5.8
	front*	only fingers	Ag-Al	3.4
	front*	only BBs	Ag2	2.4
	rear	fingers+BBs	Ag1	7.2
n-HIP-MWT+	front	fingers+pseudo-BBs	Ag-Al	3.5
	rear	fingers+BBs	Ag1	6.1
	rear	p-type contact pads	Ag-via	0.5

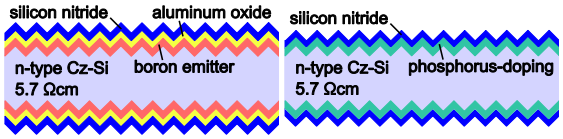

(a) $j_{0,E,pas}$-sample (b) $j_{0,BSF,pas}$-sample

Figure 5: Schematic cross sections of the symmetric lifetime samples to determine the saturation current densities (a) $j_{0,E,pas}$ of the passivated boron emitter and (b) $j_{0,BSF,pas}$ of the passivated phosphorus BSF.

3.3 Saturation current densities j_0 of the passivated surfaces and the base material

To determine the saturation current densities $j_{0,E,pas}$ of the passivated boron emitter and $j_{0,BSF,pas}$ of the passivated phosphorus BSF, symmetric lifetime samples are fabricated in parallel to the solar cells (see Fig. 5, two samples per diffusion). As base material, textured n-type Cz-Si wafers with a specific base resistivity of $\rho_{base} \approx 5.7$ Ωcm are used. The effective lifetimes are measured by QSSPC at five points for each wafer. Then, the saturation current densities j_0 are obtained by applying the j_0-analysis as in the Sinton Instruments' WCT-120 [26]. The resulting mean values are $j_{0,E,pas} \approx 76$ fA/cm² and $j_{0,BSF,pas} \approx 112$ fA/cm² (for a single side). The saturation current density of the base $j_{0,base} \approx 40$ fA/cm² is calculated according to [27] with a wafer thickness $W = 190$ µm, a base doping concentration $N_D = 3.2 \cdot 10^{15}$ cm^{-3}, and a base lifetime $\tau_{base} = 2.5$ ms.

Assuming that the total saturation current density j_{01} of the first diode in the two-diode model can be described as the sum of the single recombination paths, $j_{01} = j_{0,E,pas} + j_{0,BSF,pas} + j_{0,base} \approx 228$ fA/cm². Thus, the limit in open-circuit voltage—calculated from j_{01} by using the one-diode model with a short-circuit current density $j_{SC} = 39$ mA/cm² and a temperature $T = 25$°C—is $V_{OC,limit} \approx 665$ mV.

3.4 Proportion of metallized surface area

Table I summarizes the percentages of metallized surface area for the front and rear sides of the H-pattern and the n-HIP-MWT+ solar cells (see also Fig. 2).

The number of fingers and the finger widths are equal for both cell types on the respective side. The finger widths are measured on 15 wafers at six different positions per wafer and side. The average finger widths on the front and rear sides are 58 µm and 76 µm, respectively.

4 SOLAR CELL RESULTS

4.1 Current-voltage (*I-V*) measurements

The *I-V* characteristics of the cells with the best performance are shown in Table II. The values refer to measurements performed with black foil-coated and thus non-reflective measurement chucks [28]. The conversion efficiencies η for the H-pattern and n-HIP-MWT+ cell are 19.4 % and 19.5 %, respectively. These two cells are also measured with reflective measurement chucks. This results in a gain in short-circuit current density j_{SC} of ≈ 1 $\%_{rel}$ for both cell types, which consequently increased the conversion efficiencies by 0.2 $\%_{abs}$ to 19.6 % for the H-pattern and to 19.7 % for the n-HIP-MWT+ cell.

In the following discussion, all *I-V* data refer to the measurements performed with the non-reflective chucks, as summarized in Table II.

4.1.1 H-pattern cells

When comparing the two H-pattern cells, the advantage of a reduced Ag-Al metallization fraction on the front side by the application of non-contacting busbars is obvious. The cell with non-contacting Ag2 busbars (3.4 % Ag-Al paste metallized and contacted front area; Table II) reaches a conversion efficiency of η = 19.4 % in comparison to η = 19.1 % for the cell with contacting Ag-Al busbars (5.8 % metallized front area). This difference of 0.3 $\%_{abs}$ in η is mainly due to differences in the open-circuit voltage V_{OC}. For the cell with non-contacting Ag2 busbars, the V_{OC} is 646 mV and thus 7 mV higher compared to the other cell.

The values for the short-circuit current density j_{SC} are almost identical, as shading sums up to 5.8 % for both cells.

The fill factors *FF* are also almost identical with values close to 77 %, as the differences in *pFF* and series resistance r_S compensate for each other in the two cells. The *FF*s are mainly limited by rather low pseudo fill factors *pFF* below 81.5 %. The reasons for the overall rather low *pFF* values are currently being investigated. Whether or not higher *pFF*s of up to 0.8 $\%_{abs}$ can be expected for cells with non-contacting busbars is another subject of investigation. According to the two-diode model, the different values for parallel resistance r_P of 3.5 kΩcm² and 9.8 kΩcm² for the two cells do not explain the difference in their *pFF* values, as only a gain in *pFF* < 0.4 $\%_{abs}$ is calculated for r_P tending towards infinity. Thus, r_P is not the dominating loss term for *pFF*.

4.1.2 n-HIP-MWT+ cells

For the n-HIP-MWT+ cells, laser drilling of the vias has been performed either before or after passivation, see Fig. 3. For the cell with via drilling before passivation, a cleaning step followed the via drilling. By comparing the *I-V* data for both cells, only a minor difference is observed and the maximum achieved conversion efficiencies η are 19.4 % and 19.5 %. The cell with via drilling before passivation, and thus with wet chemical cleaning step, shows only slightly higher values in j_{SC} = 39.6 mA/cm² and V_{OC} = 650 mV compared to the other cell with j_{SC} = 39.4 mA/cm² and V_{OC} = 648 mV. This might originate from marginally changed doping profiles due to the wet chemical cleaning step for the cell with via drilling before passivation. The values for *FF*, *pFF*, r_P, and r_S are almost identical. However, the process sequence with via drilling directly before metallization is very promising with respect to process simplicity, and does not show any serious drawbacks so far.

The n-HIP-MWT+ cells benefit from a clearly higher j_{SC} (up to +0.7 mA/cm²) due to less shading compared with the H-pattern cells. Furthermore, the V_{OC} for both n-HIP-MWT+ cells is also slightly higher than for the H-pattern cell with non-contacting Ag2 busbars. Since all three cell structures feature a similar front side metallization fraction for the contacting Ag-Al paste (≈ 3.5 %; see Table II), these V_{OC} differences might originate from the lower metallization fraction on the rear side of the n-HIP-MWT+ cells (n-HIP-MWT+: 6.1 %, contacting paste Ag1; H-pattern: 7.2 %, paste Ag1 as well). Another explanation could be statistical variations in iV_{OC} of the cells prior to metallization, see section 4.2. It is particularly noteworthy that no significant negative effect of the via metallization is observed on V_{OC} for the n-HIP-MWT+ cells.

The values for *pFF* and r_P are similar to those of the H-pattern cell with contacting Ag-Al busbars. As already mentioned, the reasons for the rather low *pFF* values are currently being investigated. Regarding the r_P values, we showed in a previous work that they are limited by the front side emitter doping profile, irrespective whether the cell structure is H-pattern or n-HIP-MWT+ [13]. Hence, the increase in *pFF* and r_P is a general challenge which is not limited to one of the two cell structures specifically.

By further optimizing the grid layout, r_S is expected to decrease for next generations of n-HIP-MWT+ and H-pattern cells.

4.2 Implied open-circuit voltages iV_{OC}

For two samples per group, implied open-circuit voltages iV_{OC} have been determined prior to metallization. Fig. 6 shows the iV_{OC} as well as the V_{OC} values of these cells. By calculating the difference, the open-circuit voltage loss $\Delta V_{OC} = V_{OC}$ - iV_{OC}, caused by front and rear side metallization, can be quantified. These values are also depicted in Fig. 6. The measured iV_{OC} values range from 660 mV to 663 mV, and are thus close to the value for $V_{OC,limit}$ ≈ 665 mV, as determined in section 3.3. In section 4.1.2, it was discussed that the slightly higher V_{OC}

Table II: *I-V* data for the best n-type Cz-Si H-pattern and n-HIP-MWT+ solar cells for each variation as shown in Fig. 3 (cell area: 239 cm²). All cells are initially tested with an industrial cell tester. The two cells marked with * are measured at Fraunhofer ISE CalLab PV cells. The data refer to measurements performed with black-foil coated and thus non-reflective measurement chucks [28]. For the other two cells, the data is corrected with respect to the CalLab measurements.

Cell type	External front busbars	Laser drilling of vias	η (%)	V_{OC} (mA/cm²)	j_{SC} (mV)	*FF* (%)	*pFF* (%)	r_P (kΩcm²)	r_S (Ωcm²)
H-pattern	contacting Ag-Al	-	19.1	639	38.9	76.9	80.6	3.5	0.7
	non-contacting Ag2	-	19.4*	646	39.0	77.1	81.4	9.8	0.8
n-HIP-MWT+	-	before passivation	19.5*	650	39.6	75.7	80.4	3.8	0.9
	-	after passivation	19.4	648	39.4	75.7	80.3	2.9	0.9

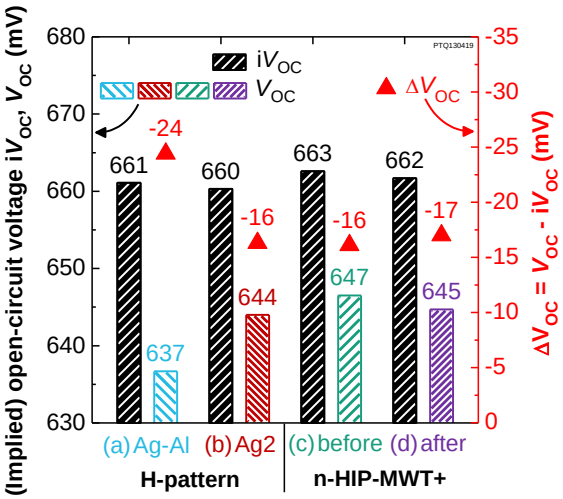

Figure 6: Left axis: mean (implied) open-circuit voltage iV_{OC}, V_{OC} of two cells per group. Right axis: loss in open-circuit voltage $\Delta V_{OC} = V_{OC}$ - iV_{OC} caused by the front and rear side metallization. Pastes for busbar metallization of the H-pattern cells: (a) contacting Ag-Al, (b) non-contacting Ag2. For the n-HIP-MWT+ cells, via drilling is performed either (c) before or (d) after passivation.

values of the n-HIP-MWT+ cells might originate from statistical variations in iV_{OC}. By looking at the iV_{OC} values in Fig. 6, this seems to be possible.

The H-pattern cells with contacting Ag-Al busbars show the highest loss with ΔV_{OC} = -24 mV. In the case of the H-pattern cells with non-contacting Ag2 busbars, the loss is only ΔV_{OC} = -16 mV, and therefore 8 mV less. This is consistent with the results in Table II. The losses of the n-HIP-MWT+ cells with ΔV_{OC} = -16/-17 mV are as high as those of the H-pattern cells with non-contacting Ag2 busbars. This shows that the reduction of the metallization fraction with the Ag-Al paste on the cell's front side leads to a significant gain in V_{OC}.

5 ESTIMATION OF METALLIZATION LOSSES

5.1 Approach

For the determination of saturation current densities $j_{0,met}$ underneath the metal contacts, an option is to perform a variation in metallization fraction F_M on cell level. For example, F_M is varied on the front side while F_M is kept constant on the rear side. Subsequently, $j_{0,met}$ - $j_{0,E,pass}$ can be extracted from the slope of the j_{01} over F_M plot [14,15,29].

In our experiment, we also performed a variation in metallization fraction F_M on the front side, namely for the H-pattern cells. As we have already shown that the Ag2 busbar paste is indeed of non-contacting nature (see also Fig. 7a,b), the cells feature two different front side metallization fractions for the contacting Ag-Al paste: F_M = 3.4 %, and F_M = 5.8 % (see Table I). This variation is sufficient for a rough estimation of $j_{0,met,Ag-Al}$ for the Ag-Al paste on the front side of our fabricated cells. Hence, also an estimation of $j_{0,met,Ag1}$ for the contacting Ag1 paste on the rear side is possible.

5.2 Results

The j_{01} values are determined by fitting the *I-V* characteristics using the two-diode model for the H-pattern cells that are discussed in section 4.2 and shown in Fig. 6. The resulting mean values are j_{01} = 422 fA/cm² (F_M = 3.4 %), and j_{01} = 505 fA/cm² (F_M = 5.8 %). Assuming that j_{01} can be described as the sum of the single recombination paths, the dependence of j_{01} on F_M is linear:

$$j_{01} = j_{0,rest} + \left(j_{0,met,Ag-Al} - j_{0,E,pas}\right) F_M, \qquad (1)$$

with

$$j_{0,rest} = j_{0,base} + j_{0,E,pas} + j_{0,BSF} \qquad (2)$$

being the value of the intersection of the regression line with the y-axis.

The slope $(j_{0,met,Ag-Al} - j_{0,E,pass})$ is calculated with linear regression using equation (1). The value for $j_{0,E,pas}$ is determined in section 3.3 to be $j_{0,E,pas} \approx 76$ fA/cm². Hence, we find the saturation current density of the front Ag-Al contact to be $j_{0,met,Ag-Al} \approx 3500$ fA/cm².

To estimate a value for $j_{0,met,Ag1}$ for the contacting Ag1 paste on the rear side, we use equation (2) and split the contributions of the metallized and non-metallized areas for $j_{0,BSF}$—the total saturation current density of the rear-side BSF—as follows:

$$j_{0,BSF} = j_{0,BSF,pas}\left(1 - F_{M,Ag1}\right) + j_{0,met,Ag1}\, F_{M,Ag1}. \qquad (3)$$

With the values given in Table I and section 3.3, the value for $j_{0,met,Ag1}$ calculates to $j_{0,met,Ag1} \approx 1100$ fA/cm².

Note that the determined values should be regarded as a rather rough estimation. Nevertheless, the results clearly indicate that the metallization losses of the front-side Ag-Al paste—used for contacting the boron emitter—are significantly larger than those of the rear-side Ag1 paste—used for contacting the phosphorus BSF. This is in agreement to results obtained by other authors [14,15,29,30].

The reasons for the significantly higher saturation current densities $j_{0,met,Ag-Al}$ below the Ag-Al contacts are currently being discussed within the PV community, as for example in ref. [14,15,31,32]. One possible explanation proposed by Edler et al. [14] is that the Ag-Al paste

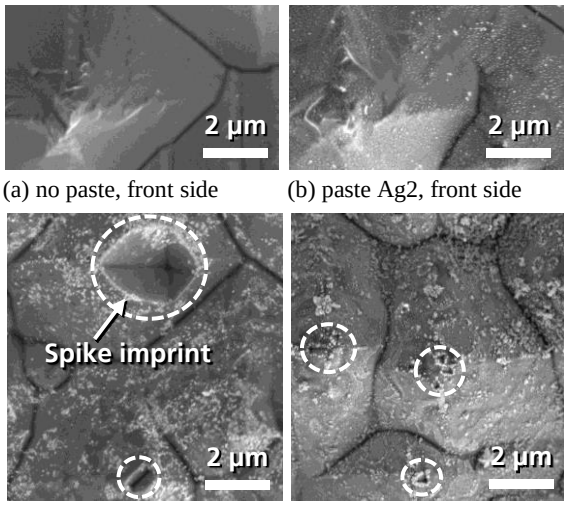

(a) no paste, front side (b) paste Ag2, front side

(c) paste Ag-Al, front side (d) paste Ag1, rear side

Figure 7: SEM images of the alkaline textured silicon surfaces after removal of finger metallization, passivation, and glass layer. (a) No metal paste was present in this area. (b) No imprints are observed for the non-contacting Ag2 paste. (c) Two imprints (a very large and a smaller one) are clearly visible for the Ag-Al paste. (d) The imprints caused by paste Ag1 are significantly smaller.

penetrates quite deeply into the emitter region. By utilizing a simplified geometrical model (that is, assuming that the metal penetrates the emitter along the whole width of the contact), they found good agreement between simulation and experimental data.

Deep penetration of Ag-Al paste into boron-doped emitters has also been observed experimentally, but rather in the form of large and thus deep spikes [31,32]. After etching away the Ag-Al paste, the passivation, and the glass layer, we also observe such large and deep spike formation. By studying the scanning electron microscope (SEM) image shown in Fig. 7c, a very large and a smaller spike imprint are visible. These spikes are significantly larger than those observed for the Ag1 paste in Fig. 7d. Roughly estimated, the larger spike at the top in Fig. 7c has a width of $w_{spike} \approx 2.5$ µm, and thus a depth of $d_{spike} \approx 1.8$ µm. The values for the smaller spike are $w_{spike} \approx 0.5$ µm, and $d_{spike} \approx 0.35$ µm. This shows that spikes originating from the used Ag-Al paste penetrate deeply into the boron emitter.

As the next section shows, deep spikes are necessary to explain the $j_{0,met,Ag\text{-}Al} \approx 3500$ fA/cm² for the Ag-Al paste by numerical simulation. In addition, deep spikes can also be a possible origin for local shunting.

6 MODELING OF METALLIZATION LOSSES

Sentaurus Device is used for numerical 2D-simulations of $j_{0,met,Ag\text{-}Al}$ underneath the Ag-Al paste. These simulations are based on calculations according to the one-diode model with the following assumptions:

- Flat wafer surface (no texture)
- Symmetrical spikes in the form of inverted pyramids
- Ohmic contact at the metal-silicon interface (no intermediate dielectric layer) with maximum surface recombination velocity $S_{met} = 10^7$ cm/s for the entire interface area

Fig. 8 depicts exemplary cross-sections of the simulation results for a spike coverage of $F_S = 50$ % and two different spike depths d_{spike} of 0.21 µm and 0.32 µm. For the deeper spike, the current density at its tip is strongly increased, which leads to a significant increase in $j_{0,met}$.

Fig. 9 summarizes the simulated $j_{0,met}$ for all performed variations in F_S and d_{spike}. Only the results obtained for $d_{spike} \leq 0.4$ µm are shown. Beyond this depth, the spike starts to locally distort the pn-junction—about 480 nm deep for our fabricated solar cells (Fig. 4)—making the calculations prone to major errors.

First, we consider the result for $d_{spike} = 0$ µm. This scenario, in which no spike formation occurs, represents

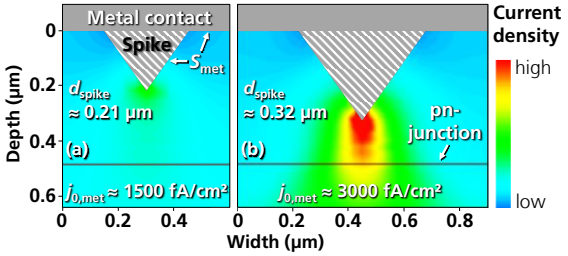

Figure 8: Cross-sections of the symmetry element of the $j_{0,met}$ simulations for $F_S = 50$ % and two d_{spike} values. The images show the electron current flow (minority carriers in the emitter region) underneath the metal contact.

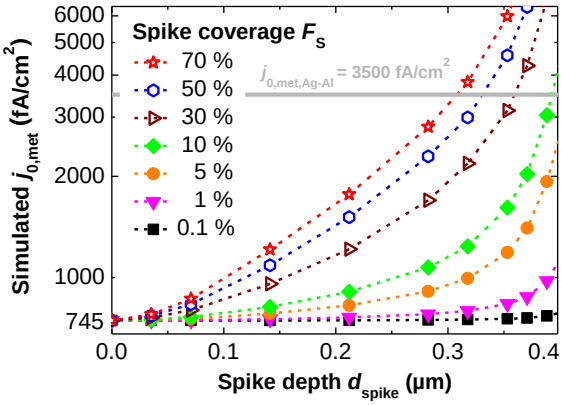

Figure 9: Results of the performed $j_{0,met}$ simulations with varied d_{spike} and F_S values. The experimentally determined $j_{0,met,Ag\text{-}Al} \approx 3500$ fA/cm² is indicated.

the simple loss of the whole passivated area below the metal contact during contact firing (no metal penetrates the boron emitter). As the simulated $j_{0,met} = 745$ fA/cm² is much smaller than the experimentally found value of $j_{0,met,Ag\text{-}Al} \approx 3500$ fA/cm², this scenario does not explain the observed V_{OC} losses on cell level.

The simulation shows two major effects of the spikes on $j_{0,met}$: i) an enlargement of the contact-surface and weakening of the emitter structure leads to a rather linear increase of $j_{0,met}$ for small spikes; ii) a culminating electron current draw over the pn-junction by the spike, which increases $j_{0,met}$ drastically for $d_{spike} \geq 0.3$ µm.

The simulated $j_{0,met}$ starts to be quantitatively consistent with the experimentally found value for $F_S > 5$ % and $d_{spike} \geq 0.3$ µm. The fewer spikes are present ($F_S \downarrow$), the deeper they have to penetrate the boron emitter ($d_{spike} \uparrow$) to create agreement between simulation and experiment. Hence, the formation of deep spikes ($d_{spike} \geq 0.4$ µm) is supposed to trigger the experimentally found $j_{0,met,Ag\text{-}Al}$ values for F_S being reasonable (see Fig. 7c).

7 CONCLUSION

We present large-area (239 cm²) high-performance metal wrap through+ (n-HIP-MWT+) solar cells on n-type Cz-Si. Besides a boron-doped front-side emitter, this approach features neither an emitter on the rear side nor inside the vias, nor a phosphorus-doping below the external p-type contact pads.

Peak conversion efficiencies of $\eta = 19.5$ % and $\eta = 19.7$ % are measured using a black and a white chuck, respectively. For the measurement with the black chuck, short-circuit current density j_{SC}, open-circuit voltage V_{OC}, and fill factor FF are 39.6 mA/cm², 650 mV, and 75.7 %, respectively. No significant negative effect of the via metallization is observed on V_{OC}. In addition, no serious drawbacks are found for the n-HIP-MWT+ cells, for which the laser drilling of the vias has been performed directly before metallization without any post treatment. This shows the n-HIP-MWT+ approach to be a promising candidate for next generation MWT solar cells using n-type Cz-Si.

For simultaneously fabricated n-type Cz-Si H-pattern cells, the decrease in area contacted with silver-aluminum (Ag-Al) paste on the boron emitter leads to a significant gain in V_{OC} of up to 8 mV. The overall losses in V_{OC}—caused by front and rear side metallization—are found to be 24 mV and 16 mV for the H-pattern cells with elec-

trical contacting and non-contacting front-side busbars, respectively. For the latter, the V_{OC} loss corresponds to the loss observed for the n-HIP-MWT+ cells.

The saturation current density below the front-side Ag-Al contact is found to be $j_{0,met,Ag\text{-}Al} \approx 3500$ fA/cm², which is three times higher than the value found for the silver contacts on the rear side ($j_{0,met,Ag} \approx 1100$ fA/cm²). The higher $j_{0,met}$ for the Ag-Al paste is assumed to correlate with deep spikes formed during contact firing. Numerical simulations also indicate that the experimentally determined $j_{0,met,Ag\text{-}Al}$ values are most likely due to the deep spike formation. Hence, the decrease of $j_{0,met}$ on the cell's front, either by improved pastes or by deeper junctions underneath the contacts, is one of the main challenges for further development.

ACKNOWLEDGEMENTS

The authors would like to thank all colleagues at the Fraunhofer ISE Photovoltaic Technology Evaluation Center (PV-TEC); especially H. Brinckheger, F. Fertig, J. Greulich, W. Hasan, R. Hoenig, M. Jahn, K. Krauß, S. Maier, R. Neubauer, M. Retzlaff, F. Schwehr, and D. Trogus. This work was funded by the German Federal Ministry for Economic Affairs and Energy within the research project "THESSO" under contract 0325491.

E. Lohmüller thanks the "Reiner Lemoine Stiftung" for funding the work within the scope of his dissertation.

REFERENCES

[1] E. Van Kerschaver, R. Einhaus, J. Szlufcik et al., "A novel silicon solar cell structure with both external polarity contacts on the back surface", *Proc. 2nd WCPEC*, Vienna, Austria, 1998, pp. 1479–1482.

[2] B. Thaidigsmann, M. Hendrichs, S. Nold et al., "P-type MWT solar cells: current status and future expectations", *Proc. 28th EU PVSEC*, Paris, France, 2013, pp. 1099–1104.

[3] E. Lohmüller, B. Thaidigsmann, S. Werner et al., "Evaluation of via pastes for p- and n-type metal wrap through (MWT) solar cells", *Proc. 27th EU PVSEC*, Frankfurt, Germany, 2012, pp. 590–595.

[4] C. J. J. Tool, E. J. Kossen, I. J. Bennett, "P-Type MWT: integrated cell and module technology", *Proc. 28th EU PVSEC*, Paris, France, 2013, pp. 1994–1997.

[5] E. Lohmüller, M. Thanasa, B. Thaidigsmann et al., "Electrical properties of the rear contact structure of MWT silicon solar cells", *Sol. Energy Mater. Sol. Cells*, submitted, 2014.

[6] W. Yin, X. Wang, F. Zhang et al., "19.6% cast mono-MWT solar cells and 268 W modules", *IEEE J. Photovoltaics*, vol. 3, no. 2, pp. 697–701, 2013.

[7] Canadian Solar, "Canadian Solar ELPS PV cells reach 21.1% efficiency". 2012.

[8] K. Bothe, R. Sinton, J. Schmidt, "Fundamental boron-oxygen-related carrier lifetime limit in mono- and multicrystalline silicon", *Prog. Photovolt.: Res. Appl.*, vol. 13, pp. 287–296, 2005.

[9] S. W. Glunz, S. Rein, J. Y. Lee et al., "Minority carrier lifetime degradation in boron-doped Czochralski silicon", *J. Appl. Phys.*, vol. 90, no. 5, pp. 2397–2404, 2001.

[10] N. Guillevin, L. J. Geerligs, R. C. G. Naber et al., "High Efficiency n-type metal wrap through Si solar cells for low-cost industrial production", *Proc. 25th EU PVSEC*, Valencia, Spain, 2010, pp. 1429–1431.

[11] N. Guillevin, B. Heurtault, L. J. Geerligs et al., "High power n-type metal-wrap-through cells and modules using industrial processes", *Proc. 28th EU PVSEC*, Paris, France, 2013, pp. 1304–1310.

[12] E. Lohmüller, B. Thaidigsmann, F. Clement et al., "Transfer of the HIP-MWT solar cell concept to n-type silicon", *Energy Procedia*, vol. 38, pp. 436–442, 2013.

[13] E. Lohmüller, F. Fertig, S. Werner et al., "Reverse bias behavior of diffused and screen-printed n-type Cz-Si solar cells", *IEEE J. Photovoltaics*, in press, 2014.

[14] A. Edler, V. D. Mihailetchi, L. J. Koduvelikulathu et al., "Metallization-induced recombination losses of bifacial silicon solar cells", *Prog. Photovolt.: Res. Appl.*, 2014.

[15] F. Kiefer, R. Peibst, T. Ohrdes et al., "Emitter recombination current densities of boron emitters with silver/aluminum pastes", *Proc. 40th IEEE PVSC*, Denver, USA, 2014, in press.

[16] Y. Schiele, S. Joos, G. Hahn et al., "Etch-back of p+ structures for selective boron emitters in n-type c-Si solar cells", *Energy Procedia*, in press, 2014.

[17] F. Fertig, S. Rein, M. Schubert et al., "Impact of junction breakdown in multi-crystalline silicon solar cells on hot spot formation and module performance", *Proc. 26th EU PVSEC*, Hamburg, Germany, 2011, pp. 1168–1178.

[18] F. Dauzou, R. Cabal, Y. Veschetti, "Electrical behaviour of n-type silicon solar cells under reverse bias: influence of the manufacturing process", *Sol. Energy Mater. Sol. Cells*, vol. 104, pp. 175–179, 2012.

[19] R. Cabal, F. Dauzou, V. Sanzone et al., "Industrial process leading to 19.1% on n-type Cz silicon", *Proc. 26th EU PVSEC*, Hamburg, Germany, 2011, pp. 1164–1167.

[20] T. Blévin, A. Lanterne, B. Grange et al., "Development of industrial processes for the fabrication of high efficiency n-type PERT cells", *Sol. Energy Mater. Sol. Cells*, in press, 2014.

[21] E. Lohmüller, S. Werner, J. Schön et al., "Depletion of boron-doped surfaces protected with barrier layers during $POCl_3$-diffusion", *Proc. 28th EU PVSEC*, Paris, France, 2013, pp. 1043–1047.

[22] E. Peiner, A. Schlachetzki, D. Krüger, "Doping profile analysis in Si by electrochemical capacitance-voltage measurements", *J. Electrochem. Soc.*, vol. 142, no. 2, pp. 576–580, 1995.

[23] A. Richter, Souren, F. M. M., D. Schuldis et al., "Thermal stability of spatial ALD deposited Al_2O_3 capped by PECVD SiN_x for the passivation of lowly- and highly-doped p-type silicon surfaces", *Proc. 27th EU PVSEC*, Frankfurt, Germany, 2012, pp. 1133–1137.

[24] M. Spitz, U. Belledin, S. Rein, "Fast inductive inline measurement of the emitter sheet resistance in industrial solar cell fabrication", *Proc. 22nd EU PVSEC*, Milan, Italy, 2007, pp. 47–50.

[25] D. B. M. Klaassen, "A unified mobility model for device simulation - I. Model equations and concentration dependence", *Solid-State Electronics*, vol. 35, no. 7, pp. 953–959, 1992.

[26] A. L. Blum, J. S. Swirhun, R. A. Sinton et al., "An updated analysis to the WCT-120 QSSPC measurement system using advanced device physics", *Proc. 28th EU PVSEC*, Paris, France, 2013, pp. 1521–1523.

[27] R. M. Swanson, R. A. Sinton, "High-efficiency silicon solar cells", *Adv. in Solar Energy: An Annual Rev. of Res. and Develop.*, vol. 6, pp. 427–484, 1990.

[28] J. Hohl-Ebinger, W. Warta, "Bifacial solar cells in STC measurement", *Proc. 25th EU PVSEC*, Valencia, Spain, 2010, pp. 1358–1362.

[29] T. Fellmeth, A. Born, A. Kimmerle et al., "Recombination at metal-emitter interfaces of front contact technologies for highly efficient silicon solar cells", *Energy Procedia*, vol. 8, pp. 115–121, 2011.

[30] A. Edler, V. D. Mihailetchi, C. Comparotto et al., "On the metallization losses of bifacial n-type silicon solar cells", *Proc. 27th EU PVSEC*, Frankfurt, Germany, 2012, pp. 1429–1431.

[31] R. Lago, L. Pérez, H. Kerp et al., "Screen printing metallization of boron emitters", *Prog. Photovolt.: Res. Appl.*, vol. 18, no. 1, pp. 20–27, 2010.

[32] F. D. Heinz, M. Breitwieser, P. Gundel et al., "Microscopic origin of the aluminium assisted spiking effects in n-type silicon solar cells", *Sol. Energy Mater. Sol. Cells*, in press, 2014.